

## Erratum

# Precise elemental and isotope ratio determination by simultaneous solution nebulization and laser ablation-ICP-MS: application to U–Pb geochronology

Ingo Horn<sup>\*</sup>, Roberta L. Rudnick, William F. McDonough

*Department of Earth and Planetary Sciences, Harvard University, Cambridge, MA 02138, USA*

Received 11 March 1999; accepted 17 August 1999

### Abstract

We have developed a procedure for precise in situ elemental and isotope ratio measurements by simultaneous solution nebulization and laser ablation inductively coupled plasma mass spectrometry, which can be applied to isotope and element ratio determinations (e.g.,  ${}^6\text{Li}/{}^7\text{Li}$ ,  ${}^{10}\text{B}/{}^{11}\text{B}$ , Ca/Sr and others) covering the entire mass range. Using a quadrupole mass spectrometer, our procedure yields precision of  $\leq 2.0\%$  (all errors are 2 sigma of the standard error) for  ${}^{206}\text{Pb}/{}^{238}\text{U}$  and  ${}^{207}\text{Pb}/{}^{206}\text{Pb}$  and  $\leq 3\%$  for  ${}^{207}\text{Pb}/{}^{235}\text{U}$  in neo-Proterozoic or older zircons and baddeleyite with U contents  $\geq 65$ –270 ppm. Importantly, this is accomplished without the use of an external calibration standard. We nebulize a solution containing known amounts of natural Tl and a  ${}^{235}\text{U}$  spike simultaneously with ablation of an unknown accessory phase. This allows precise mass discrimination correction of Pb/Pb as well as Pb/U in the ablated signal. Laser-induced elemental fractionation of Pb from U is observed to be a linear function of the number of laser pulses (crater depth) and is inversely exponentially correlated with spot size. These systematics allow us to correct for elemental fractionation. Spots with diameters  $\geq 150\ \mu\text{m}$  show no appreciable Pb/U fractionation, whereas for  $35\ \mu\text{m}$  spots U becomes progressively depleted relative to Pb, with a factor of four increase in Pb/U over a 2-min ablation period. For the Harvard standard zircon, 91 500, we obtain a  ${}^{206}\text{Pb}/{}^{238}\text{U}$  age of  $1061 \pm 4\ \text{Ma}$  and a  ${}^{207}\text{Pb}/{}^{206}\text{Pb}$  age of  $1074 \pm 8\ \text{Ma}$  (TIMS age: 1065 Ma for  ${}^{206}\text{Pb}/{}^{238}\text{U}$ , [Wiedenbeck, M., Alle, P., Corfu, F., Griffin, W.L., Meier, M., Ober, F., von Quant, A., Roddick, J.C., Spiegel, J., 1995. Three natural zircon standards for U–Th–Pb, Lu–Hf, trace element and REE analyses. *Geostand. Newsl.* 19, 1–23]); for the SHRIMP zircon standard, SL13, we obtain a  ${}^{206}\text{Pb}/{}^{238}\text{U}$  age of  $578 \pm 10\ \text{Ma}$  and a  ${}^{207}\text{Pb}/{}^{206}\text{Pb}$  age of  $595 \pm 13\ \text{Ma}$  (TIMS age: 572 Ma, [Claoué-Long, J.C., Compston, W., Roberts, J., Fanning, C.M., 1995. Two carboniferous ages: A comparison of SHRIMP zircon dating with conventional zircon ages and  ${}^{40}\text{Ar}/{}^{39}\text{Ar}$  analysis. In: *Geochronology Time Scales and Global Stratigraphic Correlation*. SEPM Special Publication, pp. 3–21],  ${}^{206}\text{Pb}/{}^{238}\text{U}$  age from SHRIMP: 580–565 Ma, [Compston, W., 1999. Geological age by instrumental analysis: The 29th Halmond Lecture. *Mineralogical Magazine* 63, 297–311]). The Phalaborwa baddeleyite is strongly reverse discordant yielding an upper intercept age of  $2057 \pm 8\ \text{Ma}$  (TIMS age: 2060 Ma, [Reischmann, T., 1995. Precise U/Pb age determination with baddeleyite ( $\text{ZrO}_2$ ), a case study from the Phalaborwa igneous complex, South Africa. *S. Afr. J. Geol.* 98, 98]; 2059.8 Ma, [Heaman, L.M., LeCheminant, A.N., Paragenesis and U–Pb systematics of baddeleyite ( $\text{ZrO}_2$ ). *Chemical Geology* 110, 95–126]) and a lower intercept at

<sup>\*</sup> Corresponding author. E-mail: horn@eps.harvard.edu

~ 0 Ma. These results demonstrate that LA-ICP-MS is capable of dating accessory phases with precision and accuracy comparable to SHRIMP. © 2000 Elsevier Science B.V. All rights reserved.

**Keywords:** Isotope ratio; Laser ablation-ICP-MS; U–Pb geochronology

## 1. Introduction

Over the past few years, understanding of laser interaction with minerals has increased rapidly, resulting in the development of laser ablation systems with controlled ablation characteristics. Laser ablation inductively coupled mass spectrometry (LA-ICP-MS) is now comparable to secondary ion mass spectrometry (SIMS) for trace element determinations (Horn et al., 1997). However, it has lagged behind high sensitivity SIMS for in situ U–Pb dating

due to the large and temporally variable elemental fractionations observed (Fryer et al., 1995; Longgerich et al., 1996a; Eggins et al., 1998a) and the difficulty in correcting for instrument induced mass discrimination. Previous attempts at in situ U–Pb dating with a single collector quadrupole ICP-MS required either a matrix matched calibration standard (zircon) (Fryer et al., 1993; Jackson et al., 1996) or SRM NIST glasses (Hirata and Nesbitt, 1995) and a single spot size applied to both standards and unknowns. Techniques, such as “active focusing”

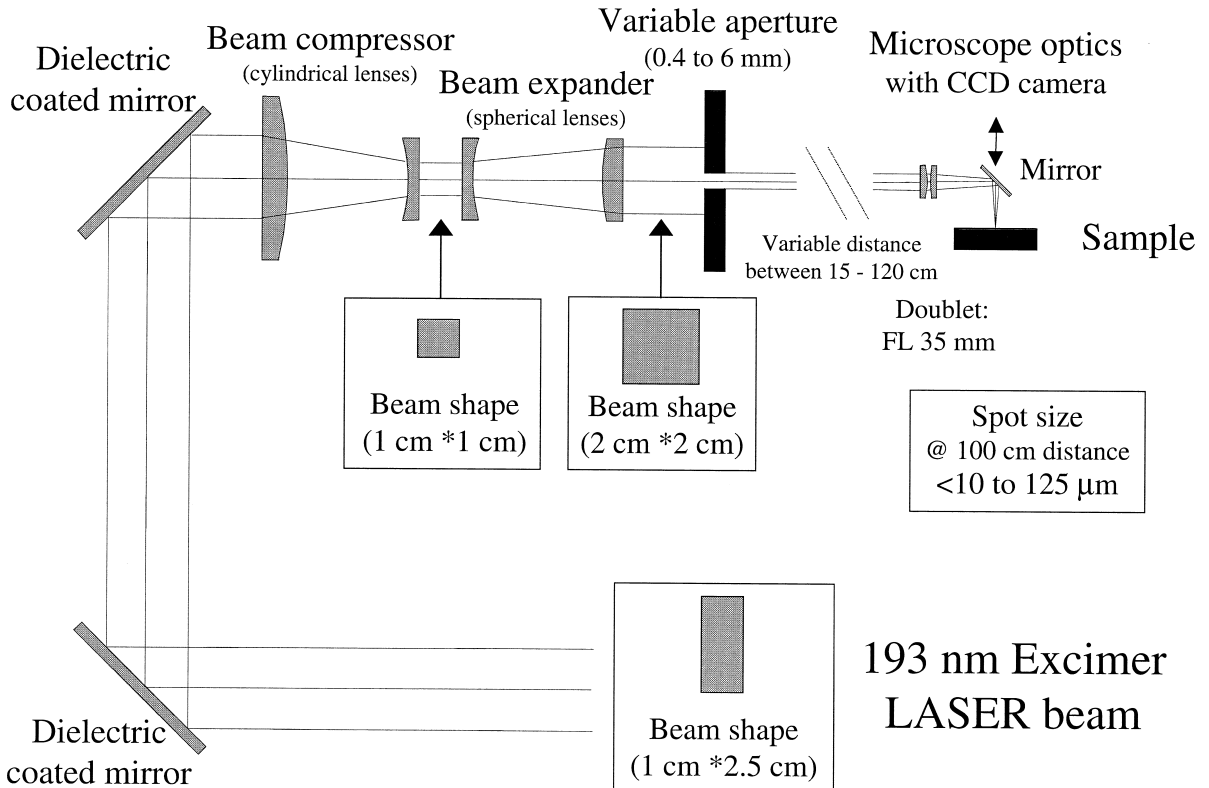


Fig. 1. Schematic of the laser beam delivery path illustrating the beam shaping and imaging of an initially rectangular excimer laser beam. The folded beam path provides a compact system with the ability to produce spot sizes of  $< 10$  to  $400\ \mu\text{m}$  while maintaining energy densities of up to  $30\ \text{J}/\text{cm}^2$  at the ablation site. If necessary, the beam expansion unit can be removed to increase the energy density by a factor of 2.5.

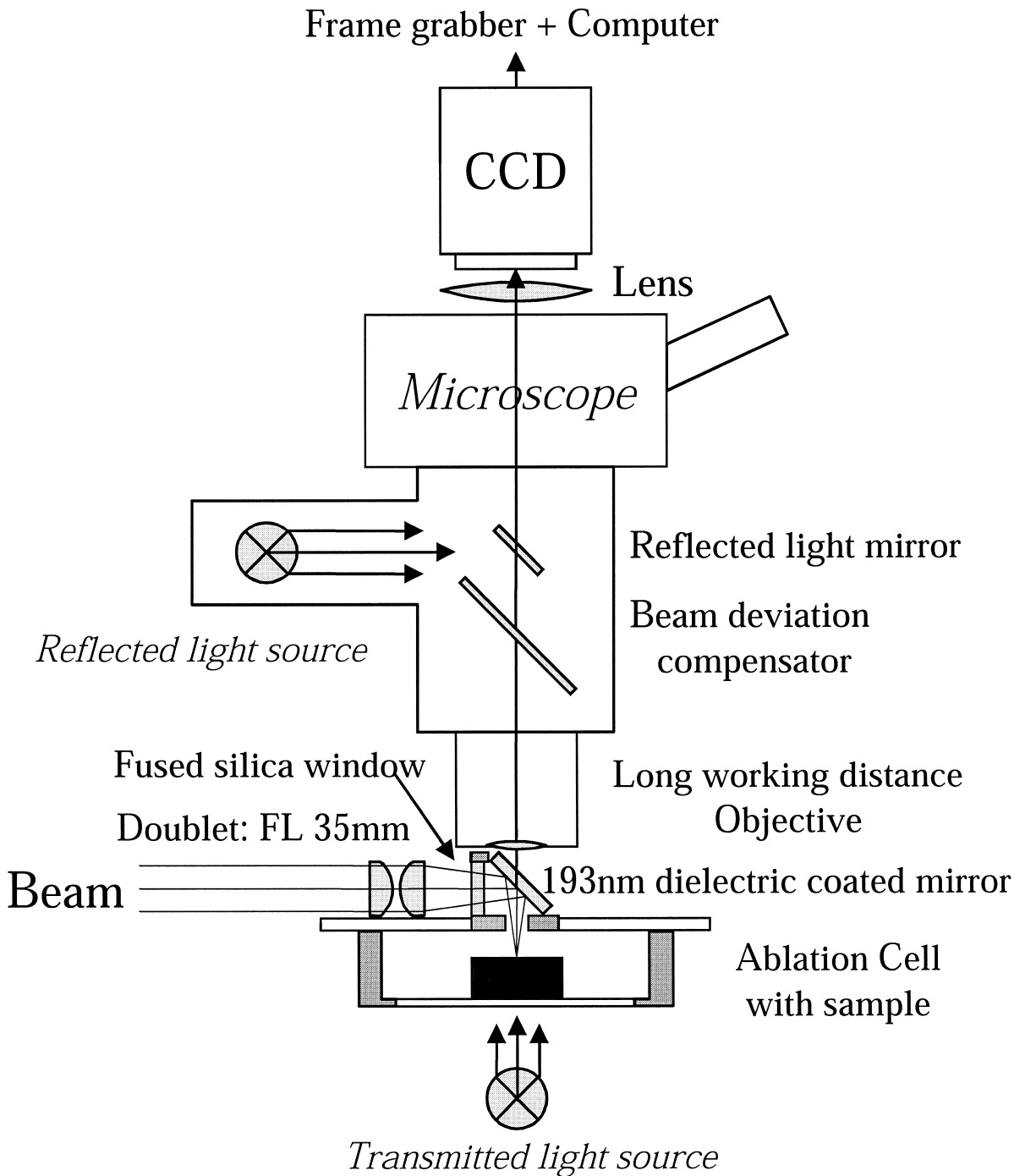


Fig. 2. The need of transmitted and axial reflected light viewing capabilities for mineral identification in conjunction with variable magnification led to separation of the laser beam path from the viewing path. Microscope magnification can be changed from  $50\times$  up to  $100\times$  when using standard long working distance objectives ( $5\times$  or  $10\times$ ) but may be increased to  $200\times$  using a  $20\times$  objective. The motorized sample positioning in conjunction with the CCD camera and frame grabber allows remote operation. The effects of chromatic aberration are minimized since no fused silica laser focusing objectives are needed for viewing.

(Hirata and Nesbitt, 1995) or soft ablation (holding the spot size constant) (Hirata, 1997) increase precision and accuracy of Pb/U ratio determinations due to reduction of laser induced elemental fractionation, but require the use of an external standard to correct for both mass discrimination and residual elemental fractionation.

In this paper, we describe a way to correct the mass discrimination of the instrument using combined solution nebulization and laser ablation sample introduction. We show that elemental fractionation is an approximately linear function of crater depth (i.e., the number of pulses applied to the sample, hence ablation time), is inversely correlated with crater diameter and is largely independent of the sample matrix. We can therefore apply a correction factor that is a function of the spot size and number of pulses applied to the sample (depth of crater). Our results for two zircon standards and a baddeleyite demonstrate that LA-ICP-MS produces precision and accuracy of U–Pb ages comparable to that of SHRIMP (Sensitive, High-Resolution Ion Microprobe).

## 2. Instrumentation and operating conditions

### 2.1. Laser

Laser ablation as a sample introduction technique in ICP-MS has been described by many authors over the past decade (Gray, 1985; Arrowsmith, 1987; Jackson et al., 1992; Fryer et al., 1995; Günther et al., 1997b; Eggins et al., 1998b). As research progressed, it was found that shorter laser wavelengths produced more controlled ablation in a variety of materials resulting in adoption of UV wavelengths (e.g., 266 nm) over the previously used IR wavelengths (1064 nm for Nd:YAG) by most ICP-MS laboratories. Quadrupled or even quintupled Nd:YAG lasers (Jeffries et al., 1998) are currently the most commonly used in geological applications. The development of excimer (excited dimer) lasers further reduced the accessible wavelength to the deep ultraviolet at 193 nm and even further to vacuum UV at 157 nm. There are currently three laser ablation systems used for trace element analysis in Earth science that employ 193 nm excimers: ANU, Aus-

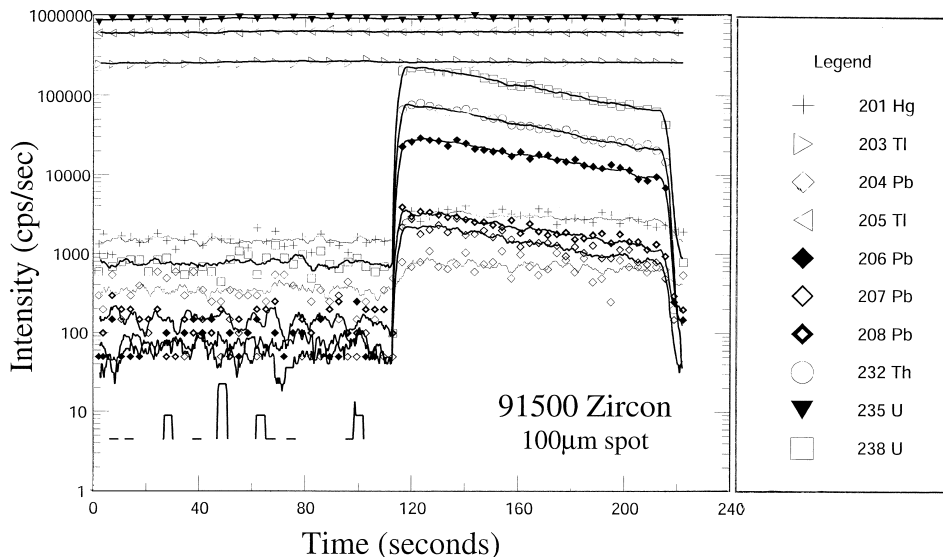


Fig. 3. Time-resolved spectrum illustrates simultaneous solid sample introduction while continuously nebulizing a solution containing Tl and  $^{235}\text{U}$ .  $^{205}\text{Tl}/^{203}\text{Tl}$  is used to correct for the mass discrimination of the Pb isotopic ratios while  $^{205}\text{Tl}/^{235}\text{U}$  of the solution signal is used to correct for mass discrimination on Pb/U. Zeros are not plotted for background counts due to the logarithmic scale; average  $^{208}\text{Pb}$  count rate in the background is 65 cps for this analysis.

tralia (Eggins et al., 1998a), ETH, Switzerland (Günther et al., 1997b); ours is the third such system.

We use a Lambda Physik excimer laser (Compex 110), using an argon fluoride gas mixture to produce 193 nm laser light with a 15-ns pulse duration. The optics system, designed and built at the Department of Earth and Planetary Sciences, Harvard University, separates the laser beam path from the viewing path (Figs. 1 and 2). The initial beam produced by this excimer laser has a maximum pulse energy of 200 mJ, and is rectangular in shape with a ratio of  $2.5 \times 1$  cm (Fig. 1). Unlike a YAG laser, it diverges in these directions at two different angles (1 mrad, and 3 mrad, respectively). This characteristic produces an ellipsoidal spot when a round aperture is imaged onto a sample, and is most obvious when spots with diameters  $< 15 \mu\text{m}$  are drilled. A set of two cylindrical lenses is used to minimize this difference in divergence angle and can be adjusted to shape the beam into a square ( $1 \times 1$  cm) that di-

verges in both directions at 3 mrad. This increases the energy density per pulse from 80 to  $200 \text{ mJ}/\text{cm}^2$ . In order to extract a homogeneous beam and reduce the energy, a beam expander is situated after the beam compressor, which produces an illuminated  $2 \times 2$  cm field of “parallel light” in front of the aperture. Twelve different sized apertures, ranging from 0.4 mm to 6 mm, are located in a carousel behind the beam expander, allowing the spot size to be varied between 8 and  $125 \mu\text{m}$ . Since the demagnification ratio can be varied by changing the distance between the masking aperture and sample (120 cm to 15 cm), a maximum spot size of  $400 \mu\text{m}$  can be achieved. After the aperture the beam is then focused with an air space doublet (35 mm focal length) onto the sample, which is contained in a cell flushed with helium (Eggins et al., 1998a). The beam passes through the cell window and is then bent  $90^\circ$  by a dielectric coated mirror positioned at  $45^\circ$  (Fig. 2).

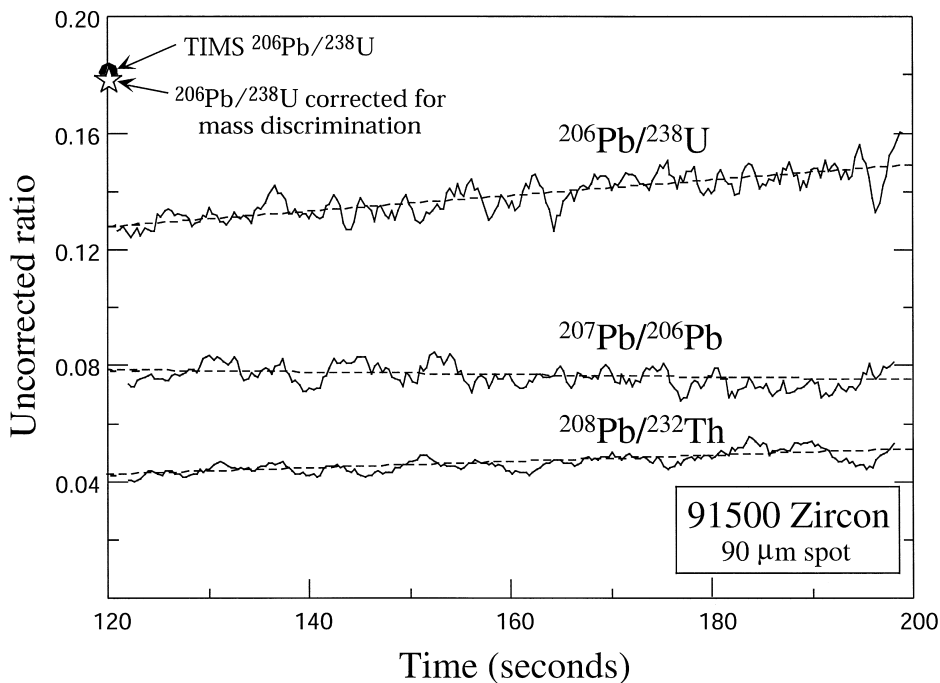


Fig. 4. Laser-induced elemental fractionation is manifested in changing Pb/U and Pb/Th with ablation time (crater depth), while the isotope ratios remain constant. Data collected at 10 Hz, 0.3 J/pulse. Data traces represent raw ratios straight from the mass spectrometer. Filled circle represents  $^{206}\text{Pb}/^{238}\text{U}$  measured by TIMS (Wiedenbeck et al., 1995) and the star represents the initial  $^{206}\text{Pb}/^{238}\text{U}$  of the ablated signal that has been corrected for instrumental mass discrimination. Note that laser was turned on  $\sim 120$  s into the analysis, after accumulation of background counts.

Laser pulse energies can be varied from  $< 60 \mu\text{J}$  to 2.5 mJ, resulting in energy densities of  $< 1$  to  $30 \text{ J/cm}^2$ . However if higher energy densities are required, or spots of  $400 \mu\text{m}$  are needed, the beam expander can be removed, allowing energy densities of up to  $80 \text{ J/cm}^2$  to be achieved. The latter are only required for ablation of optically pure materials such as fused silica or calcium fluorite. Pulse energies of 10 mJ are needed to create energy densities of  $2 \text{ J/cm}^2$  on a  $400\text{-}\mu\text{m}$  ablation site. This would produce an energy density of approximately  $0.8 \text{ J/cm}^2$  on the dielectric coated mirror following the doublet, which is still below the damage threshold of  $3 \text{ J/cm}^2$  for this optical element.

The ablation cell was modified from an original design by Sterling Shaw at Macquarie University, Sydney, Australia. It consists of a frame with a plexiglas lid bolted to the optical breadboard onto which all optical elements are mounted. The lid holds the laser objective and the mirror/cell-window assembly (Fig. 2). The sample cell forms an air-tight seal with the lid by means of suction between two O-rings. This allows movement of the sample chamber while maintaining a sealed environment for sample ablation and transport to the plasma. The design incorporates a He jet that is directed onto the site of ablation, which minimizes particle deposition around the spot and cleans the surface prior to ablation.

## 2.2. ICP-MS

The work described here was done on a 1989 vintage PQ II + quadrupole ICP-MS (VG-Elemental) with a solution nebulization sensitivity of 100 million cps (counts per second)/ppm (parts per million)/abundance at masses above 100 amu (atomic mass units). Analyses were performed in fast peak hopping mode using one point per peak with a dwell time of 6 ms and a quad settling time of 10 ms. The counting efficiency could not be improved without loss of time resolution since this vintage quadrupole RF generator requires a relatively large quad settling time. A standard sample and skimmer cone were employed. This configuration results in laser ablation sensitivity of up to 7000 cps/ppm for high mass elements from a  $40 \mu\text{m}$  spot drilled with a pulse energy of  $0.3 \text{ mJ}$  (i.e.,  $24 \text{ J/cm}^2$ ). This high sensitivity is, in part, achieved by flushing the ablation cell

with He instead of Ar (Eggins et al., 1998a), which increases sample transport efficiency and reduces deposition at the ablation site, and may also significantly enhance instrument performance by changing the plasma characteristics.

Factory-supplied time resolved software was utilized for the acquisition of each individual analysis. The procedure for the acquisition and calculation of transient signals has been described in detail by Longerich et al. (1996b). Each analysis incorporates a background acquisition interval of approximately 60 s before the laser is turned on. The total acquisition time for an analysis varied between 120 and 240 s, depending mainly on the spot size and mineral thickness. The time-resolved spectra were processed off line using a spreadsheet program to apply the background subtraction and mass discrimination, fractionation, interference and common lead corrections (modified version of LAMTRACE by Simon E. Jackson).

## 2.3. Common Pb correction

Common lead corrections are hindered by the presence of small amounts of Hg in the argon gas

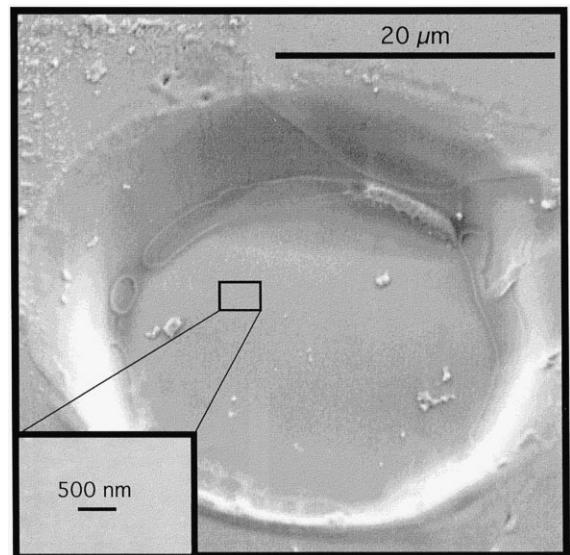


Fig. 5. SEM image of a  $\sim 30 \mu\text{m}$  crater drilled into NIST 610 glass. The inset shows a close-up of the crater floor, which is featureless at the 500 nm scale. Crater is approximately  $7 \mu\text{m}$  deep.

supply for the ICP (500 cps on  $^{202}\text{Hg}$ ), which produces an isobaric interference on mass 204 ( $^{204}\text{Hg}$  at 6.85% total Hg,  $^{204}\text{Pb}$  at 1.4% total Pb). Thus for U–Pb dating by laser ablation ICP-MS we acquire the signals of the masses 202 (Hg), 203 (Tl), 204 (Pb + Hg), 205 (Tl), 206 (Pb), 207 (Pb), 208 (Pb), 232 (Th), 235 (U) and 238 (U), and, after mass discrimination correction of the  $^{202}\text{Hg}/^{204}(\text{Pb} + \text{Hg})$  ratio, the contribution of Hg on mass 204 is subtracted (Fig. 3). However, in the analyses reported here, we did not observe  $^{204}\text{Pb}$  signals above 20 cps (corresponding to  $< 10$  ppb  $^{204}\text{Pb}$ ), which is not statistically significant. In these cases, no common lead correction was applied. The data most affected by the presence of small amounts ( $\leq 10$  ppb) of common lead are younger zircons, such as SL-13 (572 Ma). We demonstrate below by means of a Tera–Wasserburg type concordia plot that common lead was insignificant in the course of the analyses of this zircon, which may be a general case for highly crystalline zircons that have not suffered sig-

nificant radiation damage. We have recently acquired data on metamict Proterozoic zircons that contain significant quantities of common lead. In these cases the  $^{204}\text{Pb}$  correction works well (Hartz et al., unpublished analyses).

#### 2.4. General correction procedure

The raw Pb/U and Pb/Pb ratios measured by LA-ICP-MS must be corrected for two phenomena that cause deviations from the “true” ratios: (1) instrumental mass discrimination and (2) laser-induced elemental fractionation.

The first phenomenon occurs in all mass spectrometers. Plasma instruments typically show greater mass discrimination than ion microprobes or thermal ionization mass spectrometers (up to a factor of 5 higher), but, unlike the latter, the mass discrimination is constant in plasma machines as a function of analysis time, and can therefore be corrected to high precision. Instrumental mass discrimination is typi-

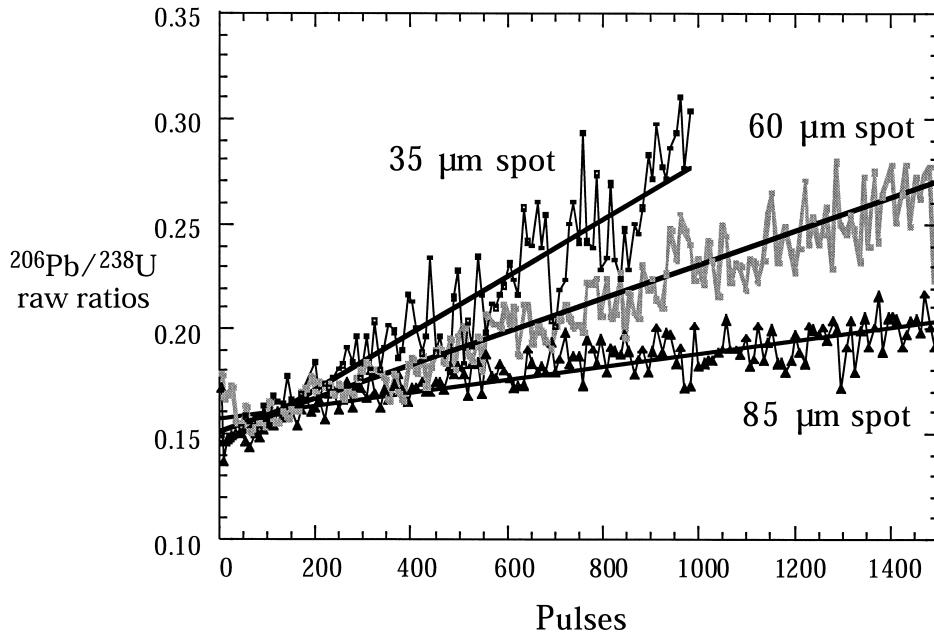


Fig. 6. Number of pulses applied vs. the uncorrected  $^{206}\text{Pb}/^{238}\text{U}$  for three different spot diameters on zircon 91500. The positive correlations illustrate that Pb/U is a linear function of crater depth. The different slopes illustrate the dependency on spot size. The slopes of the lines are a direct measure of the amplitude of elemental fractionation while the intercept depends on the isotopic composition of the sample ablated. The corrected ratio for the 91500 Zircon is 0.1792, which is nearly doubled over a depth of 50  $\mu\text{m}$  (ablation rate: 0.05  $\mu\text{m}/\text{pulse}$ ).

cally corrected by either internal normalization (e.g., in Hf and Nd isotopic analyses, where at least two isotopes are non-radiogenic), by comparison with a standard measured under the same experimental conditions (e.g., conventional TIMS Pb isotopic analyses), or, as has become common in plasma instruments, by comparison to a multi-isotopic element of similar atomic mass that is present in the analyte (e.g., using Tl isotopes to correct for Pb mass discrimination, Longerich et al., 1987). This mass discrimination appears to be generated entirely within the mass spectrometer, and has not been observed during the process of ablation, even when using a multi-collector ICP-MS (Hirata et al., 1995).

The second phenomenon, elemental fractionation, is produced at the site of ablation and has remained as one of the fundamental stumbling blocks in obtaining high precision U–Pb dates by laser ablation. However, laser-induced elemental fractionation produced in ours and the ANU excimer systems follow well-defined systematics related to the crater geometry and can thus be precisely corrected.

In the following sections, we describe the experimental procedures employed in our laboratory to correct for the effects of these two types of fractionation.

### 2.5. Instrumental mass discrimination

To correct for instrumental mass discrimination, which is generated mainly by the space charge effects in the sample-skimmer cone region and the ion transfer optics (Tanner et al., 1994), an external mass discrimination correction is applied. We achieve this by simultaneous solution nebulization and laser ablation sample introduction. This solid/liquid combination was established by Chenery and Cook (1993) and Günther et al. (1997a) as a calibration procedure for trace element determinations but has not been widely adopted (Perkins et al., 1997).

A solution containing known amounts of Tl and  $^{235}\text{U}$  (enriched to 99.9%  $^{235}\text{U}$ ) is continuously nebulized and mixed with the laser ablation signal gas flow (Fig. 3). The mixing is performed using a  $\sim 1$

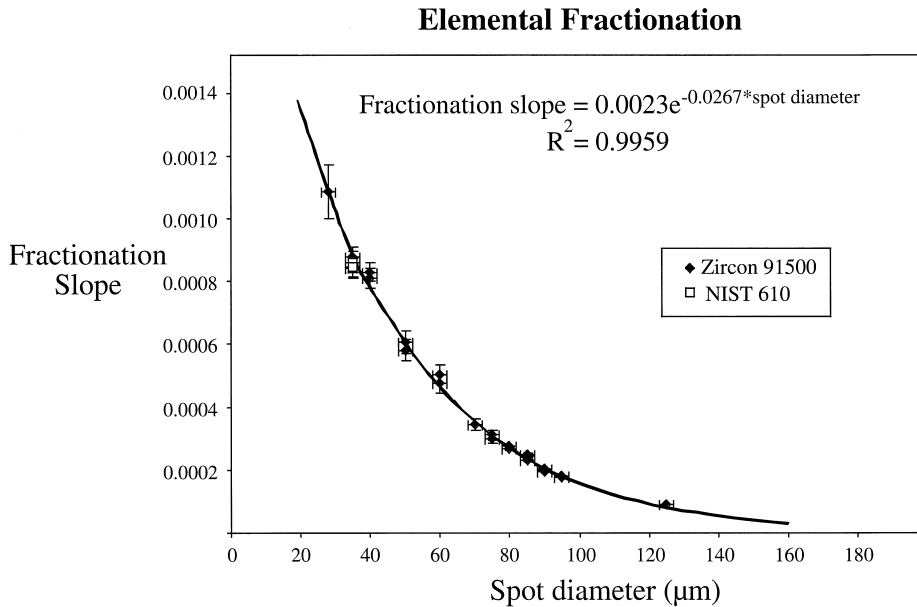


Fig. 7. Negative correlation between crater diameter (determined optically) and fractionation slope (determined from number of pulses applied vs. Pb/U plots; see Fig. 6). Curve represents fit of the slope of 30 individual time resolved analyses of the 91500 zircon and SRM NIST 610 over a wide range of spot sizes. These individual linear fits have been recalculated through an intercept of 1 to obtain a ratio independent correction. The correlation suggests that fractionation will reach a very low value for spot sizes  $> 150 \mu\text{m}$ . This correction can be applied not only to correct isotopic ratios but is also applicable to elemental concentration determinations.

cm<sup>3</sup> mixing chamber attached directly to the end of a demountable torch (Glass Expansion, Australia). The solution is nebulized using a standard Meinhard concentric nebulizer in conjunction with a water-chilled Scott-type spray chamber. The two gas flows, i.e., solution nebulization and laser ablation signal flow, are balanced to obtain a sensitivity of approximately 20–40 million cps ppm<sup>-1</sup> on Tl and <sup>235</sup>U and 3000–5000 cps/ppm at high mass on the solid analyte. The resulting gas flow rate is approximately 0.8 l/min Ar for solution nebulization. The resulting laser carrier gas is a mixture of 0.3–0.4 l/min Ar

and 0.9 l/min He flow. This balance of gas flow is needed since a Meinhard nebulizer does not operate efficiently at low flow rates and both introduction systems cannot be optimized to 100% efficiency. The technique is not sensitive to the absolute values of the gas flow rates.

Simultaneous solution nebulization introduces enhanced backgrounds for some isotopes. However, most of these can be minimized by use of ultra-clean reagents. Count rates for a blank 2% HNO<sub>3</sub> solution were found to be < 50 cps for all isotopes analyzed. For the Tl–U solution, < 300 cps were observed on

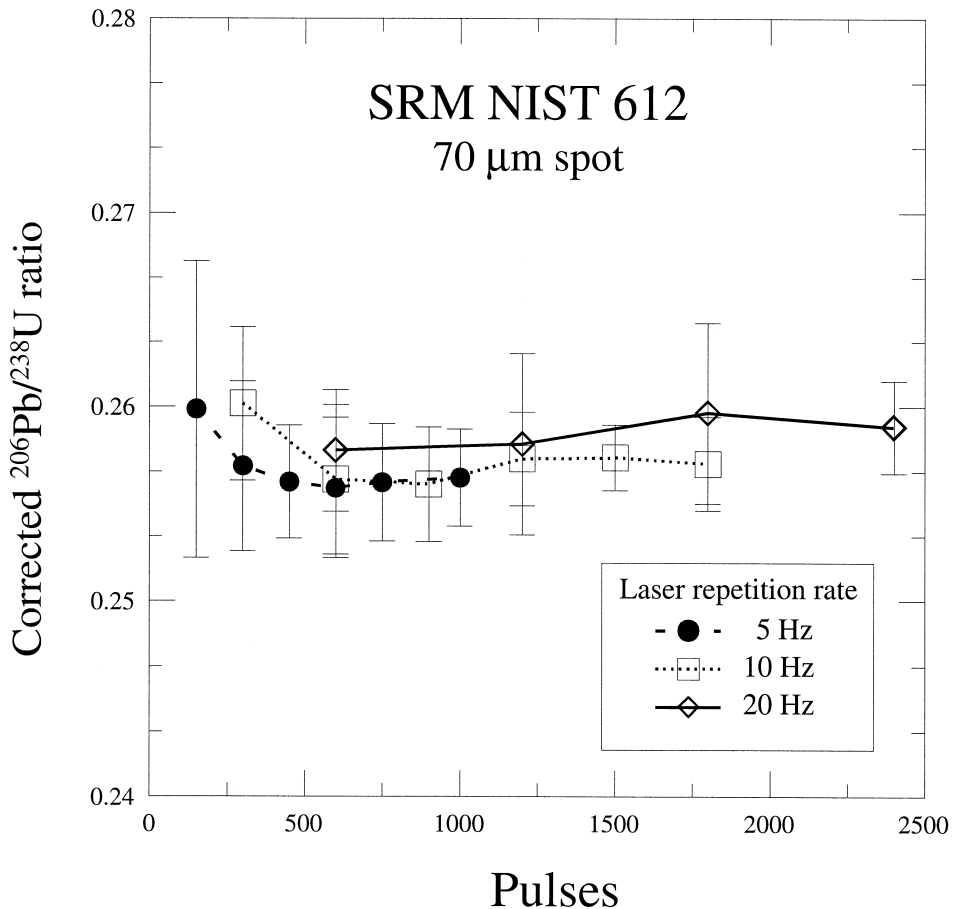


Fig. 8. Number of laser pulses vs. <sup>206</sup>Pb/<sup>238</sup>U, corrected for mass discrimination and elemental fractionation. Three experiments are shown that were carried out on NIST 612 glass using repetition rates of 5, 10 and 20 Hz at constant spot size. The flat slope indicates that fractionation is independent of pulse repetition rate for the laser wavelength of 193 nm and suggests that the fractionation is not a function of heating of the sample under these conditions. The correction procedure established using a repetition rate of 10 Hz thus applies to other repetition rates as well.

the  $^{238}\text{U}$  peak and  $< 100$  cps on the  $^{208}\text{Pb}$  peak (with a common Pb isotopic composition) (Fig. 3).

To correct the mass discrimination on the isotope ratios of Pb ( $^{207}\text{Pb}/^{206}\text{Pb}$ , etc.), the mass discrimination per amu (atomic mass unit) was determined using  $^{205}\text{Tl}/^{203}\text{Tl}$  (Longerich et al., 1987), which is assumed to be 2.3871 (Dunstan et al., 1980). This discrimination factor was found to be 0.7% per amu. After correction of the isobaric interference of Hg on  $^{204}\text{Pb}$ , the Pb isotopic ratios were corrected using the exponential law. The reliability and accuracy of using the Tl isotopic ratio to correct for mass discrimination on Pb has been established previously by several authors (Longerich et al., 1987; Walder et al., 1993; Hirata, 1998; Rehkaemper and Halliday, 1998).

Mass discrimination correction of  $^{206}\text{Pb}/^{238}\text{U}$ ,  $^{207}\text{Pb}/^{235}\text{U}$  and  $^{208}\text{Pb}/^{232}\text{Th}$  cannot be extrapolated from  $^{205}\text{Tl}/^{203}\text{Tl}$ , as the fractionation laws do not apply over such a large mass range (32 amu) in quadrupole ICP instruments. Therefore, a precisely prepared solution having  $^{205}\text{Tl}/^{235}\text{U}$  of 0.934 (verified by multi collector ICP-MS measurement in our laboratory), was used to correct for instrumental mass discrimination of Pb/U and Pb/Th, using the exponential law. The mass discrimination per amu was found to be  $1.5 \pm 0.2\%$  (over 2 h, cf. 0.7% for Pb/Pb, above), and does not change appreciably whether a power or exponential law is employed. The exact ratio of  $^{205}\text{Tl}$  to  $^{235}\text{U}$  in the solution is not important — we chose a value near one in order to maximize the precision of our measurements. Note also that other isotopes (e.g.,  $^{232}\text{Th}$ ,  $^{233}\text{U}$ ) could be used to correct for instrumental mass discrimination, depending upon availability. In any procedure, the oxide formation of U must be kept to a minimum ( $< 0.4\% \text{UO}^+/\text{U}^+$ ) since oxide production will increase the measured Tl/U and thereby influence determination of the mass discrimination.

## 2.6. Laser-induced elemental fractionation

Laser induced elemental fractionation has proved to be one of the major difficulties in determining precise isotopic ratios of elements with different volatilities such as U and Pb (Fryer et al., 1995; Hirata and Nesbitt, 1995; Longerich et al., 1996a;

Eggins et al., 1998a). The effect is manifested by a changing Pb/U ratio as a function of ablation time (Fig. 4). Pb/U ratios have been observed to vary by a factor of 3 to 4 using a Nd:YAG laser system while ablating SRM NIST 610 (Hirata, 1997). Pb/Pb ratios are obviously not affected by elemental fractionation (Fig. 4), and only require correction for instrumental mass discrimination, as described above. In the past, correction for elemental fractionation involved matrix matching between sample and calibration standard while maintaining a constant crater diameter and laser pulse energy. The latter were necessary to ensure constant energy densities during ablation. The use of a calibration standard, such as a known zircon or a NIST SRM glass, was needed to correct not only for the effect of elemental fractionation, but also to determine the mass discrimination between the Pb–Pb, Pb–U and Pb–Th isotopes.

Our excimer system delivers a flat top laser beam profile and constant energy density to the sample, which produces a near cylindrical crater for a working depth of 100 microns (Fig. 5), similar to that produced by other excimer systems (Günther et al., 1997b; Eggins et al., 1998a). Under these conditions, we observe that the fractionation of Pb/U is correlated with the depth and diameter of the crater (Figs. 6 and 7): Pb/U correlates positively with depth (number of laser pulses applied) and negatively with crater diameter. Eggins et al. (1998a) observed a similar correlation between fractionation and crater aspect ratio in the NIST 610 glass and show that the sense of the fractionation reverses itself after  $\sim 400$  to 2000 pulses are applied to the sample (depending on crater diameter). We observe a similar, but less dramatic reversal in our analyses of NIST 610, however, we do not observe a fractionation reversal in zircon or baddeleyite, where Pb/U fractionation continues linearly to great crater depths (Fig. 6). Like Eggins et al. (1998a), we do not observe a correlation between the degree of Pb/U fractionation and pulse repetition rate when using 5, 10 or 20 Hz pulse repetition rates (Fig. 8). This observation suggests that elemental fractionation in the 193 nm wavelength, unlike the 1064 nm wavelength (Outridge et al., 1996), is not a function of heating the sample, since a higher pulse repetition rate leads to higher temperatures at the site of ablation (Bäuerle, 1996).

The above correlation between element fractionation and spot geometry observed in two laboratories (ours and ANU) suggests that the laser-induced elemental fractionation we observe is related to the efficiency of element transport (volatile vs. refractory) from the crater into the plasma of the ICP. At the 193 nm wavelength, ablation is mainly photolic (i.e., non-thermal bond breaking by direct photodissociation, Bäuerle, 1996) and all elements should be liberated from the sample with the same efficiency into a vapor plume, traveling upwards at  $10^5$  to  $10^6$  cm/s (Bäuerle, 1996). We envisage that as the vapor plume cools, refractory elements (such as uranium and the REE) condense. In contrast, the highly volatile elements, such as, Pb, Bi and Zn, remain in the gas phase for a longer time due to their low condensation temperatures. Several observations support these interpretations: (1) high resolution electron microscopy reveals a smooth and featureless floor to the ablation crater at the submicron scale (Fig. 5), with no evidence of melting, consistent with material being fully vaporized by the 193 nm laser pulses, (2) elemental fractionation continues along the same slope when the laser is interrupted and restarted within a given pit after the sample has cooled significantly, and (3) the mass discrimination corrected  $^{206}\text{Pb}/^{238}\text{U}$  during the initial stages of ablation are the “true” ratios (Fig. 4), demonstrating that little

elemental fractionation has occurred at this point. The correlation between degree of element fractionation and crater depth is thus due to the preferential retention of refractory elements in the crater. This may be due to their condensation on the walls of the crater (Bäuerle, 1996; Eggins et al., 1998a) and/or due to less efficient transport of condensed particles from the ever deepening pit (Bäuerle, 1996).

The above systematics allow us to correct for the effects of elemental fractionation by a linear fit of  $^{206}\text{Pb}/^{238}\text{U}$  as a function of crater depth (the number of laser pulses applied to the sample), acquired for different spot sizes and repetition rates. The slope of the linear fit defines the magnitude of elemental fractionation and is constant for a given spot size and laser fluence. Data were collected on the 91500 zircon (Wiedenbeck et al., 1995) and the SRM NIST 610 to define the fractionation slope vs. spot size correlation shown in Fig. 7. We term this the calibration curve. The high elemental concentrations of the NIST glass ( $\sim 450$  ppm U and total Pb) allow us to minimize the errors associated with counting statistics when ablating small spot sizes. No noticeable differences in fractionation behavior between these materials were observed, indicating that the 193 nm wavelength laser system shows little or no matrix dependency. The slopes of 30 linear regressions show a strong inverse correlation with spot diameter

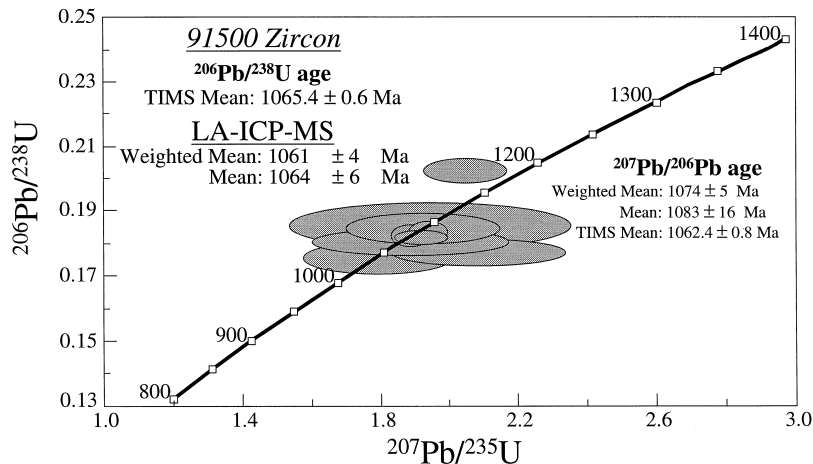


Fig. 9. Concordia diagram showing results for the 91500 zircon, with all but one spot lying on concordia. The concordant analyses yield a weighted mean  $^{206}\text{Pb}/^{238}\text{U}$  age of  $1061 \pm 4$  Ma ( $2\sigma$ ) and illustrate the accuracy and precision of the in situ technique described here. Spot sizes range from 35 to 125  $\mu\text{m}$  and correlate inversely with the size of the error ellipse, which are  $2\sigma$ . In this and subsequent diagrams the ages and errors have been calculated using K. Ludwig's program "Isoplot", version 2.12.

Table 1  
Single spot LA-ICP-MS isotope ratio and age determinations of the 91500 zircon

91500 Zircon (Ontario, Canada)		Atomic ratios							
Spot No.	208/206 Ratio	206/238 Ratio	2 $\sigma$ R.S.D. (%)	207/235 Ratio	2 $\sigma$ R.S.D. (%)	207/206 Ratio	2 $\sigma$ R.S.D. (%)	208/232 Ratio	2 $\sigma$ R.S.D. (%)
1	0.107	0.178	1.1	1.793	3.7	0.074	3.6	0.052	3.3
2	0.107	0.178	1.2	1.789	4.1	0.074	4.2	0.052	3.3
3	0.107	0.181	1.1	1.883	4.6	0.076	4.6	0.054	3.5
4	0.106	0.182	1.2	1.871	4.0	0.075	4.0	0.052	3.7
5	0.109	0.180	1.1	1.830	4.1	0.074	4.1	0.054	3.8
6	0.108	0.184	1.1	1.884	4.3	0.075	4.2	0.054	3.5
7	0.110	0.180	1.3	1.874	3.6	0.076	3.7	0.055	3.2
8	0.106	0.178	1.8	1.867	4.9	0.077	5.1	0.052	5.3
9	0.109	0.179	1.5	1.918	6.1	0.078	5.7	0.053	6.1
10	0.112	0.179	1.6	1.879	5.3	0.077	5.2	0.055	5.3
11	0.110	0.180	1.0	1.904	3.1	0.077	3.1	0.054	2.6
12	0.112	0.180	0.8	1.894	2.9	0.077	3.0	0.055	2.9
13	0.110	0.182	1.0	1.871	1.9	0.075	1.9	0.055	1.5
14	0.110	0.180	1.0	1.863	1.9	0.075	1.9	0.053	1.3
15	0.108	0.178	1.1	1.838	2.3	0.075	2.2	0.052	1.6
16	0.108	0.183	1.2	1.894	1.9	0.076	1.9	0.053	1.5
17	0.113	0.179	2.3	1.840	10.9	0.075	12.0	0.055	9.4
18	0.104	0.183	2.9	1.915	9.8	0.077	9.8	0.053	10.5
19	0.103	0.182	1.7	1.879	8.9	0.075	8.9	0.052	9.5
20	0.124	0.177	1.9	2.073	10.3	0.086	10.5	0.061	7.2
21	0.116	0.179	2.5	1.992	7.9	0.082	7.8	0.057	7.3
22	0.099	0.175	2.3	1.793	10.1	0.075	10.0	0.048	9.8
23	0.104	0.176	1.4	1.767	5.5	0.073	4.9	0.049	5.7
24	0.105	0.175	1.2	1.786	5.2	0.074	4.8	0.048	5.6
25	0.112	0.181	1.1	1.837	4.0	0.074	3.5	0.052	3.5
26	0.115	0.176	1.4	1.844	3.4	0.077	3.1	0.051	3.2
27	0.111	0.180	1.1	1.808	3.5	0.074	3.2	0.052	3.4
28	0.111	0.181	1.1	1.841	2.5	0.075	2.1	0.052	2.2
29	0.110	0.179	1.1	1.799	4.4	0.074	3.8	0.050	3.9
30	0.114	0.181	1.5	1.829	5.6	0.074	5.3	0.054	5.4
31	0.121	0.181	2.3	1.851	9.4	0.075	7.7	0.058	8.9
32	0.109	0.185	3.3	1.948	16.9	0.077	14.7	0.053	17.1
33	0.106	0.177	1.2	1.851	3.5	0.076	3.2	0.052	3.0
34	0.110	0.179	1.0	1.856	3.3	0.075	2.9	0.053	2.8
35	0.108	0.178	1.4	1.811	4.3	0.074	4.1	0.052	3.5
36	0.111	0.179	1.3	1.816	4.5	0.074	4.4	0.054	3.4
37	0.108	0.202	1.6	2.050	5.0	0.074	5.1	0.054	5.1
38	0.112	0.178	1.4	1.835	3.9	0.075	3.7	0.051	3.8
39	0.106	0.180	1.5	1.838	4.7	0.075	4.5	0.051	3.5
40	0.106	0.174	1.0	1.762	3.4	0.074	3.0	0.053	3.0
41	0.101	0.175	1.0	1.829	3.0	0.077	2.8	0.050	2.5
42	0.113	0.176	1.0	1.811	2.3	0.076	2.2	0.052	2.2
43	0.112	0.178	1.5	1.858	5.0	0.077	4.7	0.053	4.3
44	0.098	0.177	1.5	1.834	4.5	0.076	4.6	0.050	4.0
45	0.110	0.178	1.4	1.866	4.8	0.077	4.4	0.053	4.3
46	0.104	0.176	1.6	1.746	4.2	0.073	4.1	0.049	3.9
47	0.106	0.177	1.0	1.790	3.3	0.074	3.0	0.054	3.0
48	0.101	0.178	1.0	1.855	2.9	0.077	2.8	0.051	2.4
49	0.113	0.179	1.0	1.838	2.3	0.076	2.2	0.053	2.2
Weighted mean	0.109	0.179	0.41	1.844	0.84	0.07523	0.43	0.0526	1.1
Mean	0.109	0.177	1.4	1.855	1.6	0.07567	0.8	0.0524	1.6
Min.	0.098	0.174		1.746		0.073		0.048	
Max.	0.124	0.202		2.073		0.086		0.061	
TIMS <sup>a</sup>	0.1069	0.17917	0.04	1.8502	0.04	0.07488	0.01	0.05374	0.28

<sup>a</sup>Wiedenbeck et al. (1995).

Apparent age								Ablation parameters	
206/238 Age (Ma)	Mean $\pm$ 2 S.D.	207/235 Age (Ma)	Mean $\pm$ 2 S.D.	207/206 Age (Ma)	Mean $\pm$ 2 S.D.	208/232 Age (Ma)	Mean $\pm$ 2 S.D.	Ablation time (s)	Spot size ( $\mu\text{m}$ )
1058	12	1043	24	1028	37	1020	34	49.8	60
1054	13	1042	27	1032	43	1022	34	70.7	60
1073	12	1075	30	1094	51	1055	37	57.6	60
1077	13	1071	26	1078	43	1032	39	56.3	60
1069	12	1056	27	1042	43	1064	40	59.6	60
1089	12	1075	28	1064	45	1056	37	57.6	60
1066	14	1072	24	1100	40	1078	34	66.1	60
1058	19	1069	33	1112	56	1031	55	49.1	50
1063	16	1087	41	1144	66	1053	64	66.1	50
1059	17	1074	35	1118	58	1076	57	69.4	50
1067	10	1082	21	1126	35	1066	28	49.1	65
1069	8	1079	19	1114	33	1074	31	41.3	65
1080	10	1071	13	1068	20	1074	16	50.4	80
1068	11	1068	12	1080	21	1043	14	72.0	80
1058	12	1059	16	1086	24	1024	16	76.6	70
1082	13	1079	14	1054	20	1041	16	55.7	70
1062	25	1060	72	1074	129	1084	102	36.7	30
1082	31	1086	66	1114	109	1044	109	23.6	30
1075	18	1074	59	1080	96	1030	98	35.4	30
1051	20	1140	71	1342	140	1204	87	32.1	30
1061	26	1113	53	1236	96	1116	82	38.6	30
1042	24	1043	66	1058	106	956	94	41.6	30
1044	15	1034	36	1018	50	956	56	58.7	60
1038	13	1040	34	1054	50	954	53	62.1	60
1071	12	1059	26	1050	37	1016	36	69.6	60
1047	14	1061	22	1108	34	1009	32	57.3	70
1066	12	1048	23	1028	33	1032	35	56.6	70
1070	11	1060	16	1058	22	1031	23	75.8	70
1063	12	1045	29	1030	39	992	39	67.2	60
1073	17	1056	37	1044	55	1066	58	46.8	60
1074	25	1064	62	1066	82	1132	101	49.8	60
1093	37	1098	114	1130	167	1051	180	39.3	50
1053	13	1064	23	1100	35	1019	30	82.9	70
1064	11	1066	22	1080	32	1037	29	86.0	70
1058	14	1050	28	1044	43	1033	37	65.5	70
1062	14	1051	30	1044	46	1062	36	54.3	70
1187	19	1132	34	1042	53	1072	55	46.8	80
1056	15	1058	26	1078	40	1014	39	40.9	70
1065	16	1059	31	1070	48	999	35	41.6	70
1034	11	1032	22	1050	32	1052	32	85.3	80
1040	11	1056	19	1108	31	985	24	70.6	80
1045	10	1049	15	1082	23	1031	22	69.2	125
1055	16	1066	33	1110	52	1034	44	58.7	70
1050	16	1058	30	1090	50	995	40	52.9	70
1058	15	1069	32	1108	48	1038	45	71.0	70
1043	16	1026	27	1004	41	973	38	38.9	80
1049	11	1042	22	1050	32	1068	32	85.3	80
1054	11	1065	19	1108	31	999	24	70.6	80
1059	10	1059	15	1082	23	1045	23	69.2	125
1061	4	1061	9	1074	5	1034	11		
1064	6	1065	6	1083	16	1040	13		
1034		1026		1004		954			
1187		1140		1342		1204			
1065.4	0.6			1062.4	0.8	1058.1	5.6		

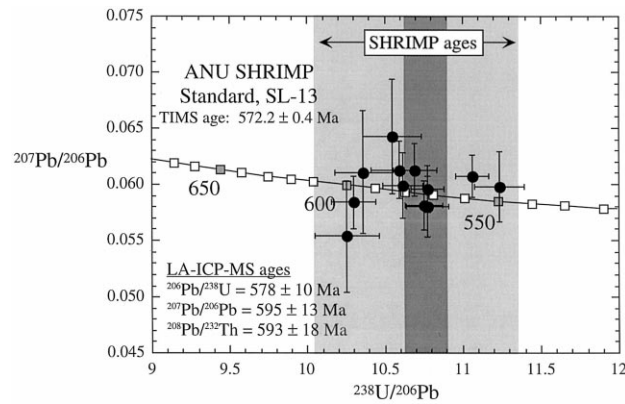


Fig. 10. Tera–Wasserberg concordia diagram showing individual spot analyses of the SL13 zircon, which has been dated by TIMS to a concordant  $^{206}\text{Pb}/^{238}\text{U}$  age of  $572.2 \pm 0.4$  Ma (Claoué-Long et al., 1995). Size of the error bars ( $2\sigma$ ) correlate with spot size — smaller errors represent  $55\ \mu\text{m}$  spots and larger errors represent  $25\ \mu\text{m}$  spots. Our results give a weighted mean  $^{206}\text{Pb}/^{238}\text{U}$  age of  $578 \pm 10$  Ma, which is within 1% of the TIMS results. New SHRIMP results reported by Compston (1999) show a significant heterogeneity in the  $^{206}\text{Pb}/^{238}\text{U}$  ages of the SL13 zircon (light gray field). Compston interpreted this zircon to have crystallized at 580 Ma followed by metamorphism at 565 Ma (dark gray band).

(Fig. 7), which is well fit by an exponential function. This plot illustrates that elemental fractionation drops to very low levels at spot sizes  $> 150\ \mu\text{m}$ , presum-

ably due to the greater efficiency of refractory element transport out of these low aspect ratio craters. The calibration curve shown in Fig. 7 was estab-

Table 2  
Single spot LA-ICP-MS isotope ratio and age determinations of the SL13 zircon

Spot No.	SL13 Zircon (Sri Lanka) Atomic ratios									
	208/206 Ratio	206/238 Ratio	$2\sigma$ R.S.D. (%)	207/235 Ratio	$2\sigma$ R.S.D. (%)	207/206 Ratio	$2\sigma$ R.S.D. (%)	208/232 Ratio	$2\sigma$ R.S.D. (%)	
1	0.026	0.0904	1.0	0.7494	3.0	0.0607	3.1	0.026	6.8	
2	0.029	0.0890	1.4	0.7274	5.4	0.0598	5.3	0.028	11.4	
3	0.027	0.0975	2.0	0.7382	8.9	0.0554	8.9	0.029	21.6	
4	0.032	0.0948	1.8	0.8338	7.7	0.0643	8.0	0.034	19.8	
5	0.027	0.0965	1.8	0.8056	8.2	0.0611	8.9	0.030	19.6	
6	0.028	0.0928	1.0	0.7558	1.8	0.0596	3.5	0.029	6.6	
7	0.026	0.0930	1.1	0.7377	3.8	0.0581	3.7	0.027	8.3	
8	0.026	0.0942	1.2	0.7721	4.7	0.0599	4.9	0.028	8.7	
9	0.041	0.0971	1.4	0.7910	3.9	0.0584	4.1	0.034	9.8	
10	0.036	0.0935	1.3	0.7981	3.6	0.0613	3.8	0.030	9.0	
11	0.040	0.0928	1.3	0.7576	4.7	0.0580	4.6	0.033	6.7	
12	0.037	0.0944	1.7	0.8058	4.4	0.0613	4.2	0.030	8.7	
Weighted mean		0.0938	1.7	0.772	2.8	0.0598	2.2	0.0298	6.0	
Mean	0.031	0.0938	1.7	0.773	2.7	0.0598	2.3	0.0299	5.7	
Min	0.0257	0.0890		0.7274		0.0554		0.0257		
Max	0.0409	0.0975		0.8338		0.0643		0.0341		
TIMS <sup>a</sup>	–	0.0928084	0.2	0.7577368	0.4	0.0592	0.3	–		

<sup>a</sup>Claoué-Long et al. (1995).

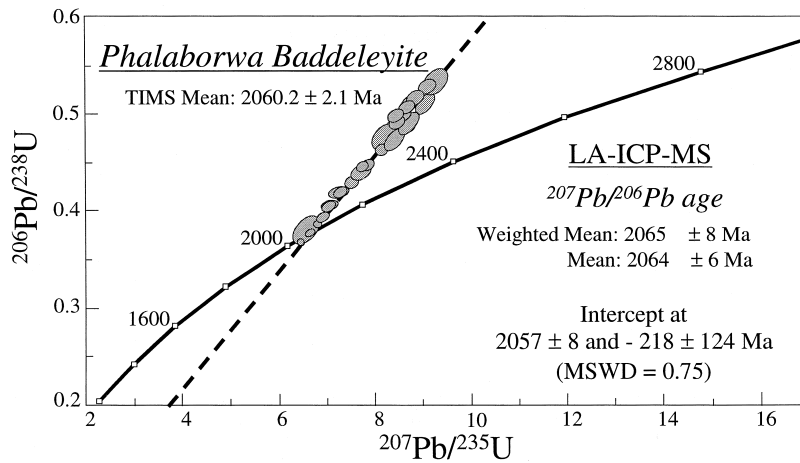


Fig. 11. Concordia diagram showing a high degree of reverse discordance for the Phalaborwa baddeleyite. Such reverse discordancy has also been observed, to a lesser degree, in TIMS analyses. An upper intercept age of  $2057 \pm 8$  Ma illustrates the accuracy of this technique when compared to the published TIMS age of 2060.4 Ma (Reischmann, 1995).

lished at the beginning of our U–Pb investigations and was applied to all data reported herein.

### 3. Results

In order to assess the reliability of the elemental fractionation and mass discrimination corrections applied to single analyses, we determined the Pb/U,

Pb/Th and Pb/Pb ratios of three different samples: zircon 91500, zircon SL13 and Phalaborwa baddeleyite. Spot sizes varied from 25  $\mu\text{m}$  to 125  $\mu\text{m}$  at a constant energy density of 2.5 J/cm<sup>2</sup>.

#### 3.1. 91500 Zircon

This sample was provided by the Harvard Mineralogical Museum. It originally consisted of one crys-

Apparent age								Ablation parameters	
206/238 Age (Ma)	Mean $\pm$ 2 S.D.	207/235 Age (Ma)	Mean $\pm$ 2 S.D.	207/206 Age (Ma)	Mean $\pm$ 2 S.D.	208/232 Age (Ma)	Mean $\pm$ 2 S.D.	Ablation time (s)	Spotsize ( $\mu\text{m}$ )
558	5	568	17	630	20	513	35	55.6	50
550	8	555	30	594	31	563	64	45.9	50
600	12	561	50	428	38	584	126	40.6	25
584	11	616	48	750	60	673	133	41.3	25
594	11	600	49	642	57	605	119	30.8	25
572	6	572	10	590	21	575	38	60.9	25
573	6	561	21	534	20	542	45	55.0	25
580	7	581	27	598	29	566	49	37.3	25
598	8	592	23	544	22	677	66	28.2	55
576	8	596	21	648	25	591	53	34.7	55
572	7	573	27	530	25	656	44	37.3	55
582	10	600	26	650	27	595	52	38.6	55
578	10	581	16	595	13	593	18		
578	10	581	12	595	51	595	32		
550		555		428		513			
600		616		750		677			
572.2	0.8	573	8			–			

tal with a mass of 238 g and has been analyzed by three different laboratories using TIMS (Wiedenbeck et al., 1995). These analyses show a consistent  $^{206}\text{Pb}/^{238}\text{U}$  age of  $1065.4 \pm 0.6$  Ma with a minor degree of discordance (Wiedenbeck et al., 1995). As a test of homogeneity this sample has also been analyzed for its isotopic composition by ion probe. Wiedenbeck et al. (1995) concluded that the sample has a homogeneous isotopic composition giving  $^{207}\text{Pb}/^{206}\text{Pb}$  of  $0.07488 \pm 1$  ( $1062.4 \pm 0.8$  Ma ( $2\sigma$ )), and mean Pb, U and Th contents of 14.9

ppm, 81.2 ppm and 28.6 ppm, respectively (Wiedenbeck et al., 1995).

Five fragments, approximately 1 mm long, were embedded in epoxy and polished prior to analysis. Results of individual spot analyses are shown in Fig. 9 and Table 1 and give a concordant mean (weighted)  $^{206}\text{Pb}/^{238}\text{U}$  age of  $1061 \pm 4$  Ma ( $2\sigma$ , 49 analyses). The average  $^{207}\text{Pb}/^{206}\text{Pb}$  of  $0.0752 \pm 3$  is in good agreement with the TIMS value. The mean  $^{208}\text{Pb}/^{232}\text{Th}$  age of  $1048 \pm 16$  Ma ( $2\sigma$ ) overlaps the TIMS value of  $1058 \pm 6$  Ma ( $2\sigma$ ). We have

Table 3

Single spot LA-ICP-MS isotope ratio and age determinations of the Phalaborwa baddeleyite

Spot No.	Phalaborwa Baddeleyite (South Africa) Atomic ratios									
	$^{208}/^{206}$ Ratio	$^{206}/^{238}$ Ratio	$2\sigma$ R.S.D. (%)	$^{207}/^{235}$ Ratio	$2\sigma$ R.S.D. (%)	$^{207}/^{206}$ Ratio	$2\sigma$ R.S.D. (%)	$^{208}/^{232}$ Ratio	$2\sigma$ R.S.D. (%)	
1	0.007	0.440	1.6	7.689	2.2	0.1282	1.5	0.118	8.9	
2	0.007	0.429	0.8	7.506	1.2	0.1281	0.9	0.135	4.5	
3	0.044	0.382	3.1	6.579	3.1	0.1264	1.1	0.083	14.4	
4	0.009	0.388	0.7	6.802	1.0	0.1286	0.8	0.136	3.7	
5	0.010	0.395	0.8	6.906	1.3	0.1282	1.1	0.120	5.1	
6	0.009	0.369	0.7	6.468	1.1	0.1286	0.8	0.129	3.9	
7	0.010	0.379	0.8	6.631	1.4	0.1282	1.1	0.115	5.4	
8	0.007	0.429	0.8	7.506	1.2	0.1281	0.9	0.135	4.5	
9	0.044	0.382	3.1	6.579	3.1	0.1264	1.1	0.083	14.4	
10	0.007	0.406	1.2	7.030	1.6	0.1270	1.3	0.095	6.5	
11	0.006	0.421	1.1	7.270	1.6	0.1270	1.3	0.121	6.0	
12	0.005	0.465	0.9	8.127	1.6	0.1282	1.7	0.177	9.3	
13	0.007	0.432	0.9	7.496	1.3	0.1275	1.1	0.131	7.1	
14	0.006	0.447	0.9	7.725	1.3	0.1274	1.2	0.092	5.9	
15	0.008	0.448	1.0	7.805	1.4	0.1282	1.2	0.091	5.8	
16	0.008	0.546	1.3	9.397	1.9	0.1271	1.6	0.136	9.5	
17	0.006	0.493	1.1	8.548	1.5	0.1280	1.1	0.124	7.7	
18	0.006	0.495	1.2	8.418	2.3	0.1258	1.7	0.140	11.5	
19	0.005	0.542	1.1	9.340	2.0	0.1273	1.7	0.148	10.5	
20	0.007	0.521	1.5	8.975	2.1	0.1268	1.4	0.116	9.8	
21	0.007	0.507	2.8	8.831	3.0	0.1286	1.1	0.118	6.5	
22	0.008	0.459	1.7	8.091	2.3	0.1299	1.6	0.156	8.6	
23	0.006	0.541	1.6	9.325	2.6	0.1269	1.6	0.146	11.4	
24	0.006	0.493	1.8	8.559	3.5	0.1283	2.7	0.136	15.6	
25	0.005	0.524	1.2	8.950	1.8	0.1262	1.1	0.123	10.8	
26	0.007	0.471	2.0	8.088	2.6	0.1264	1.4	0.122	9.9	
weighted Mean		discord.	–	discord.	–	0.1276	0.4	discord.	–	
Mean						0.1276	0.3			
Min.	0.0049	0.3685		6.4679		0.1258				
Max.	0.0435	0.5459		9.3973		0.1299				
Average (TIMS) <sup>a</sup>		discord.	–	discord.	–	discord.	discord.	–		

<sup>a</sup>Reischmann (1995).<sup>b</sup>intercept age.

determined the Pb, U and Th concentrations (by comparison to NIST 610 and using  $^{29}\text{Si}$  as an internal standard) to be 14, 65 and 31 ppm, respectively.

### 3.2. ANU SHRIMP standard zircon SL13

To correct for instrumental drift and mass discrimination using SHRIMP, the laboratory at ANU uses the SL13 zircon as a calibration standard. Matrix effects are generally high for ion microprobes so that a good matrix match between sample and standard is usually required. The SL13 zircon is a gem

quality zircon from Sri Lanka. Three groups have analyzed 19 separate chips using TIMS to establish its reference composition (Claoué-Long et al., 1995). The sample has been considered homogeneous, showing a concordant  $^{206}\text{Pb}/^{238}\text{U}$  TIMS age of  $572.2 \pm 0.4$  Ma ( $2\sigma$ ). However, more recent, high precision, SHRIMP analyses reveal heterogeneity beyond analytical errors (as manifested by high MSWD) and on the basis of this, Compston (1999) has suggested that SL13 initially crystallized at 580 Ma followed by Pb loss at 565 Ma (yielding an average bulk age of 572 Ma).  $^{206}\text{Pb}/^{238}\text{U}$  ages for 50 indi-

Apparent age								Ablation parameters	
206/238 Age (Ma)	Mean $\pm$ 2 S.D.	207/235 Age (Ma)	Mean $\pm$ 2 S.D.	207/206 Age (Ma)	Mean $\pm$ 2 S.D.	208/232 Age (Ma)	Mean $\pm$ 2 S.D.	Ablation time (s)	Spot size ( $\mu\text{m}$ )
2349	37	2195	49	2072	31	2247	199	38.2	65
2300	18	2174	26	2072	19	2564	115	68.9	65
2084	64	2057	64	2048	22	1609	231	68.9	65
2111	15	2086	22	2078	16	2570	95	86.3	110
2144	17	2099	28	2072	23	2282	117	67.9	110
2022	15	2042	22	2078	16	2451	95	86.3	110
2071	17	2064	28	2072	23	2196	118	67.9	110
2300	18	2174	26	2072	19	2564	115	68.9	110
2084	64	2057	64	2048	22	1609	231	68.9	65
2194	22	2115	14	2056	24	1834	115	90.4	95
2263	20	2145	14	2056	24	2311	131	68.2	95
2460	17	2245	14	2074	30	3287	283	44.3	95
2315	17	2173	12	2062	20	2482	165	73.7	95
2380	18	2200	12	2062	20	1778	100	61.8	95
2387	20	2209	13	2072	22	1753	96	51.2	95
2808	30	2378	18	2058	26	2586	230	37.5	50
2582	24	2291	13	2070	20	2366	172	59	50
2592	25	2277	20	2040	30	2665	287	33.1	50
2791	25	2372	19	2060	30	2796	275	31.4	50
2701	32	2335	19	2052	26	2218	207	59	50
2645	62	2321	27	2078	20	2249	138	54.6	50
2436	35	2241	21	2096	28	2931	235	40.3	50
2789	37	2370	24	2054	30	2748	292	35.2	50
2582	37	2292	32	2074	48	2583	378	25.9	50
2715	26	2333	16	2044	20	2342	239	75.4	50
2489	42	2241	24	2048	26	2322	217	83.2	50
2057 <sup>b</sup>	8	2057 <sup>b</sup>	8	2065	8	discord.	–		
				2064	6	discord.	–		
2022		2042		2040					
2808		2378		2096					
2060.5	1.5	2060.5	1.5	2060.2	2.1				

vidual spots spread between 545 and 610 Ma (Fig. 11b of Compston, 1999).

We have analyzed one chip of SL13 using spot sizes of 55 and 25  $\mu\text{m}$ . The resulting data are plotted in a Tera–Wasserburg concordia diagram (Fig. 10) and are listed in Table 2. Our results indicate a concordant mean (weighted)  $^{206}\text{Pb}/^{238}\text{U}$  age of  $578 \pm 10$  Ma ( $2\sigma$ , 12 analyses) which lies within error of the published TIMS results. We determined the  $^{208}\text{Pb}/^{232}\text{Th}$  age to be  $593 \pm 18$  Ma ( $2\sigma$ ). Our measured  $^{207}\text{Pb}/^{206}\text{Pb}$  of  $0.0598 \pm 0.0022$  agrees with the TIMS value of  $0.059247 \pm 0.000068$ . These results support previous observations that this zircon has no significant common lead component. SHRIMP's  $^{206}\text{Pb}/^{238}\text{U}$  reproducibility on SL13 over a full day's run duration is reported to be 2.34% (Claoué-Long et al., 1995) which is matched by our LA-ICP-MS results (1.6%). Age heterogeneity, as described by Compston (1999), is apparent in the scatter of ages for individual spots, which closely matches that observed by SHRIMP (Fig. 10).

### 3.3. Phalaborwa baddeleyite

This sample is from the Phalaborwa igneous complex in South Africa. TIMS analyses show a wide spread of discordance with an upper intercept age of  $2060.5 \pm 1.9$  Ma (Reischmann, 1995) and  $2059.8 \pm 0.8$  Ma (Heaman and LeCheminant, 1993), which is interpreted as the igneous crystallization age (Reischmann, 1995).

Our data reveal a far higher degree of discordance on the 35–120  $\mu\text{m}$  size scale. We have determined the upper intercept age to be  $2058 \pm 11$  yielding a lower intercept of  $\sim 0$  Ma. This age agrees well with published data and confirms the crystallization age of Heaman and LeCheminant (1993) and Reischmann (1995). The mean  $^{207}\text{Pb}/^{206}\text{Pb}$  age of  $2064 \pm 5.3$  Ma is slightly higher than that reported by TIMS. Many of the analyses are reverse discordant, a phenomenon that is more commonly observed in situ analyses than conventional analyses, and is attributed to the redistribution of radiogenic Pb on a micron scale (Williams et al., 1984; Compston, 1999). The large degree of reverse discordance, which is only in part observed by TIMS, may indicate heterogeneity at a scale of  $< 50$   $\mu\text{m}$  or an

incomplete correction of elemental fractionation (for example, if the calibration curve in Fig. 7 does not strictly hold for baddeleyite). The latter will not compromise the intercept age observed, but rather move the analyses up and down a discordia. Analyses using large spot sizes with minimized correction of elemental fractionation plot closer to concordia, but this observation does not exclude either of the above interpretations (Fig. 11, Table 3).

## 4. Comparison with SHRIMP

The results presented above illustrate that quadrupole-based LA-ICP-MS is capable of measuring U–Pb ages in zircon with precision and accuracy comparable to SHRIMP. However, differences exist between the two techniques that should be considered when evaluating which technique is best for a given application.

### 4.1. Efficiency, sensitivity and material consumed

The efficiency (ions detected per total atoms released) of the quadrupole ICP-MS is lower than that of SHRIMP. We estimate the efficiency at 0.04% for high mass elements in our system, compared with 1% for SHRIMP (Compston, 1999). This lower efficiency is, in part, compensated for by the faster sampling rate of the laser, which leads to higher sensitivity (cps/ppm). Horn et al. (1997) report that a quadrupole ICP-MS with the ‘‘S’’-option is  $\sim 200$  times more sensitive than a Cameca 3F ion probe. Sensitivity for  $^{206}\text{Pb}$  in our system is 620 cps/ppm for a 25  $\mu\text{m}$  spot and 1900 cps/ppm for a 50  $\mu\text{m}$  spot, compared to  $\sim 0.8$  cps/ppm for a ‘‘typical’’ SHRIMP spot (Compston, 1999).

Ablation rates for our system are between 0.5 and 1  $\mu\text{m}/\text{s}$  (at 10 Hz pulse repetition rate), with a typical analysis lasting for 60–120 s (depending on the thickness of the accessory mineral). In contrast, the sputtering rate in SIMS is  $\sim 1$  nm/s, with a typical spot analysis lasting 15 min. Thus, significantly more material is consumed during laser ablation than by SHRIMP (0.1 to 10  $\mu\text{g}$  quantities vs. 2 ng, respectively), but analysis times are shorter.

#### 4.2. External standardization

We have demonstrated that there is no need for external standardization for U–Pb determinations by LA-ICP-MS, provided the calibration curve (i.e., the relationship between spot diameter and Pb/U fractionation slope) has been determined for a given laser fluence (Fig. 7). We have not observed this calibration curve to differ between glass and zircon and preliminary work, applying this curve to date baddeleyite, monazite, allanite, titanite and gadolinite, yields the correct ages for these minerals (unpublished data). However, the application of this technique to different minerals may require establishment of individual calibration curves. In contrast, SIMS requires the simultaneous measurement of ma-

trix-matched, homogeneous standards due to differences in sputtering efficiency between different minerals.

#### 4.3. Depth profiling and time-resolved data acquisition

The slower drilling rates used in SIMS make it superior to LA-ICP-MS for high resolution depth profiling and analysis of thin (< 15  $\mu\text{m}$ ) rims. In contrast, the ability to acquire time-resolved data in LA-ICP-MS is an advantage over SIMS. This allows the operator to determine when zones with significantly different U, Pb and Th concentrations are penetrated during the analysis period. It also allows one to “see” when significantly metamict regions

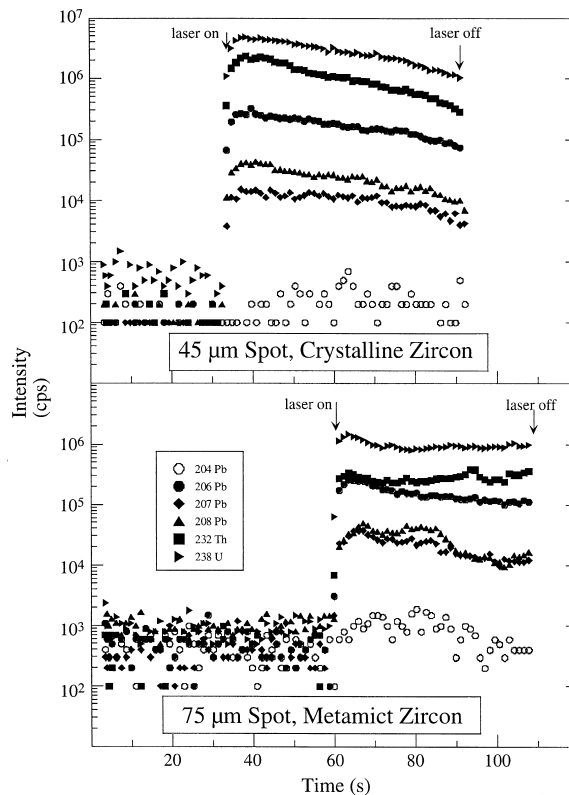


Fig. 12. Two time-resolved spectra showing variations in signal intensity that exist in zircons of variable degree of crystallinity. Upper: signal intensity from 45  $\mu\text{m}$  spot in slightly discordant zircon with a  $^{206}\text{Pb}/^{238}\text{U}$  age of 420 Ma (sample defines a discordia between 1850 and 400 Ma) illustrates the smooth signal intensity that is characteristic of homogenous, inclusion-free, non-metamict (crystalline) zircons. Note subparallel line traces. Lower: signal intensity from metamict, strongly discordant zircon with significant variation in Pb, U and Th contents within different zones (sample defines discordia between 1850 and 400 Ma). Note crossing line traces. Both analyses accumulated at 10 Hz pulse repetition rate. Zeros are not plotted for background counts due to the logarithmic scale. (Samples courtesy of Ebbe Hartz).

are sampled or when cracks containing common Pb are penetrated (Fig. 12).

#### 4.4. Cost and availability

Quadrupole-based LA-ICP-MS is about an order of magnitude less expensive than a ion microprobe with U–Pb capabilities. Consequently, many more laboratories are equipped with LA-ICP-MS facilities that can be used to great advantage for in situ U–Pb age determinations.

### 5. Conclusions

We have demonstrated that a combined solution nebulization and laser ablation sample introduction technique is an accurate and precise microanalytical tool for in situ isotope ratio determinations in minerals. The combined solid/liquid sample introduction method allows us to correct for mass discrimination independent of the sample matrix, using the  $^{205}\text{Tl}/^{203}\text{Tl}$  and the  $^{205}\text{Tl}/^{235}\text{U}$  ratio of the solution. Correction for laser-induced elemental fractionation can be made when the ablation system is designed to maintain a constant energy density on the ablation site and produces holes of a near cylindrical shape. In this case, the elemental fractionation is observed to correlate positively with crater depth and negatively with crater diameter. We attribute this to a continuously decreasing probability of particle transport of condensed matter (refractory elements) from the deepening hole to the ICP-MS. Volatile elements remain longer in the gas phase and are therefore more efficiently transported to the ICP. A systematic change of the observed fractionation behavior is expected between different volatile elements correlating with their condensation temperatures.

Using this technique, we demonstrate analytical precision of  $\sim 2\%$  RSD for Proterozoic zircons with U concentrations of  $> 80$  to 280 ppm, which is comparable to that obtained by SHRIMP.

We anticipate that the technique will be improved by (1) using a  $^{233}\text{U}$  spike for U-rich samples, which would allow for direct determination of  $^{207}\text{Pb}/^{235}\text{U}$  instead of recalculating it from  $^{238}\text{U}$ , (2) employing a desolvating microconcentric nebulizer, which would maintain dry plasma conditions, and (3) employing a

magnetic sector, multicollector ICP, which could yield precision similar to TIMS.

### Acknowledgements

We thank Steve Eggins, Trevor Ireland, Fernando Corfu, Urs Schärer and an anonymous reviewer for comments that helped to clarify and strengthen the manuscript, Ebbe Hartz for permission to illustrate his unpublished zircon analyses (Fig. 12) and Yuan Lu for the SEM images in Fig. 5. Nick Arndt is thanked for his efficient editorial handling. [NA]

### References

- Arrowsmith, P., 1987. Laser ablation of solids for elemental analysis by inductively coupled plasma mass spectrometry. *Anal. Chem.* 59, 1437–1444.
- Bäuerle, D., 1996. *Laser Processing and Chemistry*, Springer, Bern, 649 pp.
- Chenery, S., Cook, J.M., 1993. Determination of rare earth elements in single mineral grains by laser ablation microprobe-inductively coupled plasma-mass spectrometry — preliminary study. *J. Anal. At. Spectrom.* 8, 299–303.
- Claoué-Long, J.C., Compston, W., Roberts, J., Fanning, C.M., 1995. Two Carboniferous ages: a comparison of SHRIMP zircon dating with conventional zircon ages and  $^{40}\text{Ar}/^{39}\text{Ar}$  analysis. In: *Geochronology Time Scales and Global Stratigraphic Correlation*. SEPM Special Publication, pp. 3–21.
- Compston, W., 1999. Geological age by instrumental analysis: the 29th Haldom Lecture. *Mineral. Mag.* 63, 297–311.
- Dunstan, L.P., Gramsch, J.W., Barnes, I.L., Purdy, W.C., 1980. The absolute abundance and the atomic weight of a reference sample of thallium. *J. Res. Natl. Bur. Stand.* 85, 1–10.
- Eggins, S.M., Kinsley, L.P.J., Shelley, J.M.M., 1998a. Deposition and element fractionation processes during atmospheric pressure laser sampling for analysis by ICPMS. *Appl. Surf. Sci.* 127–129, 278–286.
- Eggins, S.M., Rudnick, R.L., McDonough, W.F., 1998b. The composition of peridotites and their minerals: a laser-ablation ICP-MS study. *Earth Planet. Sci. Lett.* 154, 53–71.
- Fryer, B.J., Jackson, S.E., Longerich, H.P., 1993. The application of laser ablation microprobe inductively coupled plasma-mass spectrometry (LAM-ICP-MS) to in situ (U)–Pb geochronology. *Chem. Geol.* 109, 1–8.
- Fryer, B.J., Jackson, S.E., Longerich, H.P., 1995. The design, operation and role of the laser-ablation microprobe coupled with an inductively coupled plasma-mass spectrometer (LAM-ICP-MS) in earth sciences. *Can. Mineral.* 33, 303–312.
- Gray, A.L., 1985. Solid sample introduction by laser ablation for inductively coupled plasma source mass spectrometry. *Analyst* 110, 551–556.

- Günther, D., Cousin, H., Magyar, B., Leopold, I., 1997a. Calibration studies on dried aerosols for laser ablation-inductively coupled plasma mass spectrometry. *J. Anal. At. Spectrom.* 12, 165–170.
- Günther, D., Frischknecht, R., Heinrich, C.A., Kahlert, H.-J., 1997b. Capabilities of an Argon Fluoride 193 nm excimer laser ablation inductively coupled plasma mass spectrometry microanalysis of geological materials. *J. Anal. At. Spectrom.* 12, 939–944.
- Heaman, L.M., LeCheminant, A.N., 1993. Paragenesis and U–Pb systematics of baddeleyite (ZrO<sub>2</sub>). *Chem. Geol.* 110, 95–126.
- Hirata, T., 1997. Soft ablation technique for laser ablation-inductively coupled plasma mass spectrometry. *J. Anal. At. Spectrom.* 12, 1337–1342.
- Hirata, T., 1998. Lead isotopic analyses of NIST standard reference materials using multiple collector inductively coupled plasma mass spectrometry coupled with a modified external method for mass discrimination effect. *The Analyst* 212, 1407–1411.
- Hirata, T., Nesbitt, R.W., 1995. U–Pb isotope geochronology of zircons: evaluation of the laser probe inductively coupled plasma-mass spectrometry technique. *Geochim. Cosmochim. Acta* 59, 2491–2500.
- Hirata, T., Hattori, M., Tanaka, T., 1995. In situ osmium isotope ratio analyses of iridosmines by laser ablation-multiple collector-inductively coupled plasma mass spectrometry. *Chem. Geol.* 144, 269–280.
- Horn, I., Hinton, R.W., Jackson, S.E., Longerich, H.P., 1997. Ultra trace element analysis of NIST SRM 616 and 614 using laser ablation microprobe inductively coupled plasma mass spectrometry (LAM-ICP-MS): a comparison with secondary ion mass spectrometry (SIMS). *Geostand. Newsl.* 12, 191–203.
- Jackson, S.E., Longerich, H.P., Dunning, G.R., Fryer, B.J., 1992. The application of laser-ablation microprobe-inductively coupled plasma mass spectrometry (LAM-ICP-MS) to in situ trace element determinations in minerals. *Can. Mineral.* 30, 1049–1064.
- Jackson, S.E., Longerich, H.P., Horn, I., Dunning, G.R., 1996. The application of laser ablation microprobe (LAM)-ICP-MS to in situ U–Pb zircon geochronology. *Journal of Conference Abstracts (V.M. Goldschmidt Conf.)* 1, 283.
- Jeffries, T.E., Jackson, S.E., Longerich, H.P., 1998. Application of a frequency quintupled Nd:YAG source ( $\lambda = 213$  nm) for laser ablation ICP-MS analysis of minerals. *J. Anal. At. Spectrosc.* 13, 935–940.
- Longerich, H.P., Fryer, B.J., Strong, D.F., 1987. Determination of lead isotope ratios by inductively coupled plasma-mass spectrometry (ICP-MS). *Spectrochim. Acta* 42B, 39–48.
- Longerich, H.P., Günther, D., Jackson, S.E., 1996a. Elemental fractionation in laser ablation inductively coupled plasma mass spectrometry. *Fresenius' J. Anal. Chem.* 355, 538–542.
- Longerich, H.P., Jackson, S.E., Günther, D., 1996b. Laser ablation inductively coupled plasma mass spectrometric transient signal data acquisition and analyte concentration calculation. *J. Anal. At. Spectrom.* 11, 899–904.
- Outridge, P.M., Doherty, W., Gregoire, D.C., 1996. The formation of trace element-enriched particulates during laser ablation of refractory materials. *Spectrochim. Acta Part B* 51, 1451–1462.
- Perkins, W.T., Pearce, N.J.G., Westgate, J.A., 1997. The development of laser ablation ICP-MS and calibration strategies: examples from the analysis of trace elements in volcanic glass shards and sulphide minerals. *Geostand. Newsl.* 21, 175–190.
- Rehkaemper, M., Halliday, A.N., 1998. Accuracy and long-term reproducibility of lead isotopic measurements by multiple-collector inductively coupled plasma mass spectrometry using an external method for correction of mass discrimination. *Int. J. Mass Spectrom. Ion Processes* 181, 123–133.
- Reischmann, T., 1995. Precise U/Pb age determination with baddeleyite (ZrO<sub>2</sub>), a case study from the Phalaborwa igneous complex, South Africa. *S. Afr. J. Geol.* 98, 98.
- Tanner, S.D., Cousins, L.M., Douglas, D.J., 1994. Reduction of space charge effects using a three-aperture gas dynamic vacuum interface for inductively coupled plasma-mass spectrometry. *Appl. Spectrosc.* 48, 1367–1378.
- Walder, A.J., Platzner, I., Freedman, P.A., 1993. Isotope ratio measurement of lead, neodymium and neodymium-samarium mixtures, hafnium and hafnium-lutetium mixtures with a double focusing multiple collector inductively coupled plasma mass spectrometer. *J. Anal. At. Spectrom.* 8, 19–23.
- Wiedenbeck, M., Alle, P., Corfu, F., Griffin, W.L., Meier, M., Ober, F., von Quant, A., Roddick, J.C., Spiegel, J., 1995. Three natural zircon standards for U–Th–Pb, Lu–Hf, trace element and REE analyses. *Geostand. Newsl.* 19, 1–23.
- Williams, I.S., Compston, W., Black, L.P., Ireland, T.R., Foster, J.J., 1984. Unsupported radiogenic in zircon: a cause of anomalously high Pb–Pb, U–Pb and Th–Pb ages. *Contrib. Mineral. Petrol.* 88, 322–327.